Finite-amplitude regimes of the short-wave Marangoni-Benard convective instability

P. Colinet and J. C. Legros
Université Libre de Bruxelles, Microgravity Research Center (MRC), 50, avenue F. D. Roosevelt, Code Postal 165, 1050 Bruxelles, Belgium

Y. Kamotani
Case Western Reserve University, 10900 Euclid Avenue, Cleveland, Ohio 44106

P. C. Dauby and G. Lebon
Université de Liège, Institut de Physique, B5, Sart Tilman, B-4000 Liège, Belgium
(Received 6 January 1995)

A model of the infinite Prandtl number thermocapillary instability in layers of infinite depth is developed in the framework of the amplitude equations formalism. Making use of eigenfunctions at a given Marangoni number Ma as a basis for the nonlinear problem, rather than the neutral stability functions, it is shown that third-order equations may visibly be extrapolated rather far above the threshold. In particular, results are obtained about the wavelength selection problem between fastest growing modes (wave numbers around $k_{\max} \sim \mathrm{Ma}^{1/2}$ for a zero free surface Biot number) and critical modes ($k_c \to 0$ and $\mathrm{Ma}_c \to 0$). Transient numerical integration of the equations reveals an unbounded growth of the mean wavelength, thus indicating the absence of an intrinsic wavelength for this physical system. This is explained in terms of the mean (horizontally averaged) temperature profile distortion by convection. The final steady state of this evolution (imposed wavelength) is then approximated analytically. Earlier results about the competition between rolls and hexagonal patterns are qualitatively recovered. These solutions are then investigated in the limit $\mathrm{Ma} \to \infty$, where power law relationships are derived for main convective quantities. In particular, a saturation behavior is obtained for a quantity (the bulk temperature decrease), which can be considered as a measure of the heat transport increase due to convection.

PACS number(s): 47.20.Dr, 47.20.Ky, 47.54.+r, 47.27.Te

I. INTRODUCTION

Marangoni convection usually refers to the motions generated at an interface between two fluid phases when the system is driven out of equilibrium by some imposed temperature (or mass concentration) gradients. These motions are induced by the corresponding interfacial tension gradients, to the extent that interfacial tension depends on temperature (or concentration), and if the adjacent fluids are viscous, they can extend relatively far into the bulk phases. A distinction is generally drawn between two (mutually nonexclusive) cases: the first happens when the driving flux is parallel to the interface, the second when it is perpendicular to it. Since no rest (i.e., purely diffusive) state exists for the former case, motions occur for every value of the constraint (and transitions between steady and more complex flows are generally observed when increasing the constraint [1,2]). In contrast, a purely diffusive state does exist when the flux is perpendicular to the interface and is known to become linearly unstable above a critical value of this flux [3,4].

It is this second situation (the so-called Marangoni-Bénard instability) that forms the subject of this paper. When the threshold of instability is exceeded, various dissipative structures are experimentally observed, some of them localized near the interface, in the form of small cells eventually embedded in larger convective structures [5], solitonlike propagating waves [6], or interfacial turbulence [7]. In other conditions, Marangoni-Bénard convection is rather similar to the classical buoyancy induced Rayleigh-Bénard convection [8–11], with patterns extending far into the bulk of surrounding liquids and actually reaching (and influenced by) the boundaries of the experimental vessel. Note that these apparently different forms of convection generally result in substantial increases of heat and/or mass transfer through the interface.

A well-studied Marangoni-Bénard configuration is that of a liquid layer of thickness h lying on a heated conducting rigid plate and with its upper surface in contact with an inert gaseous phase. Experimental [12] and theoretical [13] evidence suggests that the relevant dimensionless parameter expressing the critical conditions is the Marangoni number $\mathrm{Ma} = -\sigma_T \beta h^2/\mu\kappa$, where σ_T is the surface tension variation with temperature, β is the thermal gradient amplitude, μ is the dynamic viscosity, and κ is the thermal diffusivity. Note that experimental results show that the relevance of Ma may be discussed for the different case of the steady-oscillatory transition occurring in configurations where the imposed gradient is parallel to the interface [2].

Figure 1 reproduces the neutral stability results of Pearson [13] for this problem, as well as results obtained by Scanlon and Segel [14] in the case of a layer of infinite depth (the length h appearing in Ma then represents an arbitrary length). At a given Ma, perturbations with

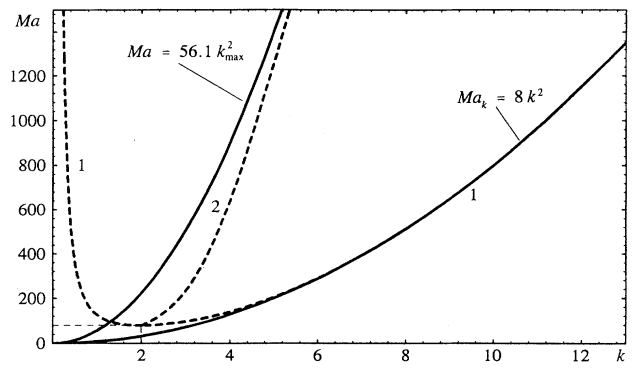

FIG. 1. Linear stability results (curves 1, neutral stability boundaries; curves 2, loci of fastest growing wave numbers) for the finite-depth case (dotted curves) and the infinite-depth case (solid curves), for a zero Biot number. The critical conditions for the finite-depth case are defined by the critical Marangoni number $\mathrm{Ma}_c=79.6$ and the critical wave number $k_c=1.99$. Formulas (infinite-depth case) are given for the neutral stability curve Ma_k [Eq. (14)] and for the locus of the fastest growing wave number $k_{\max}$ [Eq. (15)].

wave numbers in the range lying above the neutral stability curve possess a positive amplification rate. There also exists a particular wave number $k_{\max}$ in this range, which possesses the maximal amplification rate. In slightly supercritical conditions ($\mathrm{Ma}\simeq\mathrm{Ma}_c$), $k_{\max}$ is close to the critical wave number k_c and does indeed predict the size of convective (hexagonal) cells observed experimentally. When Ma is increased, $k_{\max}$ is seen to increase and the prediction of the selected wavelength becomes quite complicated since it involves nonlinear competition between modes in the unstable range. Progress has recently been achieved in this direction by Bestehorn [15]. For Ma increasing further, $k_{\max}$ can be made as large as desired compared to the critical wave number k_c (Fig. 1). This has been physically explained by the larger inertia of fluid to set in motion for lower wave-number structures [7].

In the present work, we address the question of the existence of some stable, finite amplitude regime (steady or even periodic in time) dominated by the fastest growing perturbation. After all transients have been damped out, will the convective structure be localized near the interface (as is the case for linear perturbations with $k\simeq k_{\max}$) or will it be depth scaled ($k\simeq k_c$), as in the weakly nonlinear regime? The fundamental interest of this question is related to the study of the similarities existing between nonequilibrium instabilities and equilibrium phase transitions [16]. As some equilibrium phenomena, some "nonequilibrium phase transitions" can be characterized by intrinsic wavelengths, such as the Turing instability in reaction-diffusion systems [17] or the Kelvin-Helmoltz instability in hydrodynamics [18]. For these instabilities, the stability boundary possesses a minimum of the control parameter at a finite wave number independent of the actual experiment size. It is seen in Fig. 1 that this is not the case for the Marangoni-Bénard instability (the critical wave number in a finite layer of depth h scales as $1/h$, such as for the Rayleigh-Bénard instability). However, we may conjecture that this does not rule out the possibility of an intrinsic wavelength, linked to the presence of faster growing modes (as it seems to be the case for the Rayleigh-Taylor instability [19]). Note that the finite wave number of the fastest growing mode generally depends on the driving force amplitude (the thermal gradient in our case). Attempts to answer to the question of the preference of such modes at a given supercritical driving force obviously have to incorporate nonlinear effects in the analysis.

After describing the model in Sec. II, in which the derivation of weakly nonlinear results is also presented, we discuss this wave-number selection problem for a two-dimensional geometry (rolls) and in the case where the Prandtl number can be considered infinite (the possibility of boundary-layer instabilities [20], although not observed in our analysis, is also briefly discussed). This is done in Sec. III. Buoyancy effects will be neglected, in order to concentrate on the effects of thermocapillarity. Calculations are achieved for a semi-infinite system [14] (i.e., ignoring the presence of a rigid lower boundary and thus focusing on interfacial short-wavelength effects). This simplification allows us to obtain approximate analytical results (Sec. IV) about the convective heat transfer far from the threshold and about other relevant quantities such as interfacial velocities and surface temperature variations. We end this section by extending some of these results to three-dimensional disturbances and reconsidering the problem of the competition between rolls and hexagonal convective structures.

II. PROBLEM FORMULATION AND WEAKLY NONLINEAR RESULTS

We consider a semi-infinite viscous Boussinesquian incompressible fluid in contact with an inert gas phase. The interface is located at the $z=0$ coordinate plane of a Cartesian reference frame with unit vectors $\vec{1}_i$ ($i=x,y,z$) and is assumed undeformable (this will allow obtention of analytical results and is justified since interfacial deformation is known to primarily affect long-wavelength modes [21,22]). The fluid is located in the domain $z<0$ and a constant heat flux is injected into the system (a constant temperature gradient $-\beta$ is maintained at $z\rightarrow-\infty$). All equations and boundary conditions are scaled by d (an arbitrary length) for length, d^2/κ for time, βd for temperature, and $\mu\kappa/d^2$ for pressure. The Marangoni number $\mathrm{Ma}=-\sigma_T\beta d^2/\mu\kappa$ is defined with respect to the length d, instead of the fluid thickness h ($h/d\rightarrow\infty$). Let $\vec{V}=\vec{V}_r+W\vec{1}_z$ be the fluid velocity ($\vec{V}_r$ is the horizontal velocity), T the temperature, and p the pressure perturbations with respect to the purely conductive (zero velocity) reference solution. A solution vector U will then be defined by

$$U(\vec{r}=x\vec{1}_x+y\vec{1}_y,z,t)=\begin{bmatrix}\vec{V}_r\\ W\\ p\\ T\end{bmatrix}, \tag{1}$$

which is assumed to belong to a certain set, say, E, of sufficiently derivable functions satisfy the boundary conditions of the problem: these are

$$\vec{V}_r, W, DT, p \to 0 \quad \text{for } z \to -\infty \ , \tag{2}$$

$$W = DT + \mathrm{Bi}T = 0 \quad \text{for } z = 0 \ , \tag{3}$$

where D is the dimensionless z derivative and Bi is the free surface Biot number $\mathrm{Bi} = \alpha d / \lambda$ (α is the free surface heat transfer coefficient and λ the thermal conductivity of the fluid).

The system of partial differential equations for the solution vector U can be written under the general operational form

$$\mathcal{L}(U) = \mathrm{Ma} M(U) + \Theta \left(\frac{\partial U}{\partial t} \right) + N(U, U) \ , \tag{4}$$

where the linear part $\mathcal{L}(U)$ is given by

$$\mathcal{L}(U) = \begin{bmatrix} \Delta \vec{V}_r - \vec{\nabla}_r p \\ \Delta W - Dp \\ DW + \vec{\nabla}_r \cdot \vec{V}_r \\ \Delta T + W \\ [D\vec{V}_r]_{z=0} \end{bmatrix} , \tag{5}$$

the "evolution part" is defined as

$$\Theta(U) = \begin{bmatrix} 0 \\ 0 \\ 0 \\ T \\ 0 \end{bmatrix} , \tag{6}$$

and the "constraint part" is given by

$$M(U) = \begin{bmatrix} 0 \\ 0 \\ 0 \\ 0 \\ -[\vec{\nabla}_r T]_{z=0} \end{bmatrix} . \tag{7}$$

Finally, the bilinear form N is expressed as

$$N(U_1, U_2) = \begin{bmatrix} 0 \\ 0 \\ 0 \\ \vec{V}_1 \cdot \vec{\nabla} T_2 = \vec{V}_{1r} \cdot \vec{\nabla}_r T_2 + W_1 D T_2 \\ 0 \end{bmatrix} . \tag{8}$$

In the above relations, $\vec{\nabla}_r = \vec{1}_x (\partial/\partial x) + \vec{1}_y (\partial/\partial y)$ is the horizontal gradient, $\vec{\nabla} = \vec{\nabla}_r + \vec{1}_z D$ is the total gradient, and $\Delta = \vec{\nabla}^2$ is the Laplacian operator.

Apart from the fact that pressure is not directly eliminated from the equations, the set of equations (4) together with boundary conditions (2) and (3) is equivalent to the problem formulation of Scanlon and Segel [14]. Note also that we have included the Marangoni condition as the last component of (4), which has already been shown to simplify the process of deriving amplitude equations [14,23–26].

A. Derivation of amplitude equations

We first decompose U into Fourier modes

$$U(\vec{r}, z, t) = \int U_{\vec{k}}(z, t) \exp(i\vec{k} \cdot \vec{r}) d\vec{k} \tag{9}$$

so that horizontal Fourier components $U_{\vec{k}}$ all belong to E [i.e., fulfill boundary conditions (2) and (3)] and satisfy

$$\mathcal{L}_{\vec{k}}(U_{\vec{k}}) = \mathrm{Ma} M_{\vec{k}}(U_{\vec{k}}) + \Theta_{\vec{k}} \left(\frac{\partial U_{\vec{k}}}{\partial t} \right) + \int N_{\vec{k}', \vec{k} - \vec{k}'}(U_{\vec{k}'}, U_{\vec{k} - \vec{k}'}) d\vec{k}' \ , \tag{10}$$

which is obtained by projecting (4) on $\exp(-i\vec{k} \cdot \vec{r})$ and by replacing $\vec{\nabla}_r$ by $i\vec{k}$ in linear operators (this is the meaning of the index $\vec{k}$). The bilinear form N is defined in a similar way. Each Fourier mode is further decomposed as

$$U_{\vec{k}}(z, t) = A_{\vec{k}}(t) U_k^a(z) + U_k^D(z, t) \ , \tag{11}$$

where $U_k^a(z)$ is an eigenvector with eigenvalue σ_k ($k = |\vec{k}|$) of the linear spectral problem

$$\mathcal{L}_{\vec{k}}(U_k^a) - \mathrm{Ma} M_{\vec{k}}(U_k^a) = \sigma_k \Theta_{\vec{k}}(U_k^a) \ . \tag{12}$$

The resolution of (12), detailed in Appendix B, shows that for any $\mathrm{Ma} > 0$, $0 < k < \mathrm{Ma}/2\,\mathrm{Bi}$, an isolated eigenvalue σ_k exists (and is such that $\sigma_k + k^2 > 0$). This eigenvalue is the growth rate of the corresponding eigenmode $U_k^a(z)$, appearing in Eq. (11). For every value of Ma and k, there also exists a continuum of solutions of (12) that are bounded for $z \to -\infty$ (and correspond to eigenvalues $\sigma \le -k^2$). This infinite set of solutions could eventually be used to develop the remainder term $U_k^D(z, t)$ of Eq. (11) (the superscript D stands for "damped"), but it turns out to be simpler to compute U_k^D directly, by a method explained in Appendix A. As exchange of stability holds in our problem [27], eigenvalues σ_k are real and satisfy

$$\mathrm{Ma} = \frac{2}{k} \left[-2k\sigma^{-2} + \frac{\sigma^{-1} + 2k^2\sigma^{-2} + 2k\,\mathrm{Bi}\,\sigma^{-2}}{\mathrm{Bi} + \sqrt{\sigma + k^2}} \right]^{-1} . \tag{13}$$

The neutral stability condition is found by the limit of Eq. (13) for $\sigma \to 0$:

$$\mathrm{Ma}_k = 8k(k + \mathrm{Bi}) \ , \tag{14}$$

which is the asymptotic form ($k \to \infty$) of the neutral stability condition of Pearson [13], as also seen in Fig. 1. A relation between the maximal eigenvalue $\sigma_{\max}$, $k_{\max}$, and Ma may be found by differentiating (13) at constant Ma, setting $\partial\sigma/\partial k = 0$. This gives, for Bi=0, for example,

$$\sigma_{\max} = 2(1 + \sqrt{2}) k_{\max}^2 = \alpha\,\mathrm{Ma} \text{ with } \alpha \simeq 0.086 \text{ (for Bi=0)} . \tag{15}$$

Although analytical results can also be obtained for $\mathrm{Bi} \neq 0$, they are not reproduced here for conciseness. As

remarked by Scanlon and Segel [14], the minimum (critical) value of Ma for which instability occurs is zero, due to the absence of stabilization by a rigid lower boundary of the modes with increasingly large wavelength. However, due to their large inertia, the growth rate of these modes is vanishingly small for all Marangoni numbers. This is depicted in Fig. 2: it is seen that modes with wave numbers between 0 and $k^*=(\mathrm{Ma}/8)^{1/2}$ (for $\mathrm{Bi}=0$) are unstable, so that their amplitude $A_{\vec{k}}(t)$ in the decomposition (11) show grow exponentially in time, as long as nonlinear effects can be neglected. In fact, it is shown in Appendix A that the amplitudes $A_{\vec{k}}(t)$ obey evolution equations of the form

$$\frac{\partial A_{\vec{k}}}{\partial t}=\sigma_k A_{\vec{k}}+\int Z_{\vec{k}'\vec{k}} A_{\vec{k}'} A_{\vec{k}-\vec{k}'}\,d\vec{k}' + \int\int Z_{\vec{k}'\vec{k}''\vec{k}} A_{\vec{k}'} A_{\vec{k}''} A_{\vec{k}-\vec{k}'-\vec{k}''}\,d\vec{k}'\,d\vec{k}'' \ . \quad (16)$$

These equations are strictly valid near threshold. When the Marangoni number is increased, higher-order terms should be included. Equation (16) may then be considered as resulting from a truncated modified Galerkin scheme [15,25]. Another hypothesis underlying the derivation of (16) is that the dynamics of damped modes (i.e., of $U_{\vec{k}}^D$) is determined by the evolution of the "primary" modes $A_{\vec{k}}(t)U_{\vec{k}}^q$ (this amounts to neglecting time derivatives of damped modes). This slaving principle [25,26,28], strictly valid near the threshold, is here assumed to be qualitatively valid in the strongly nonlinear regime. This can be partly justified by the fact that damped modes cannot bifurcate ($\sigma<-k^2$), as large as Ma can be (see also [33]).

Despite these assumptions, our model is expected to reflect physical reality even far from threshold provided the eigenmodes $U_{\vec{k}}^q$ are used for the Galerkin basis rather than the neutral stability functions $U_{\vec{k}}^0$. In order to illustrate the differences between these different approaches, we now turn to the derivation of weakly nonlinear results [14,23–26], for which the latter option is sufficient.

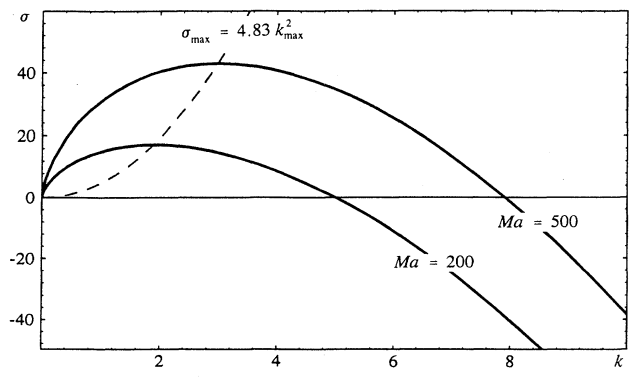

FIG. 2. Growth rate σ as a function of the wave number k for different Marangoni numbers Ma and for $\mathrm{Bi}=0$. The dotted line represents the locus of the fastest growing perturbations, given by Eq. (15).

B. Weakly nonlinear results

Making use of $U_{\vec{k}}(z,t)=A_{\vec{k}}(t)U_{\vec{k}}^0(z)+U_{\vec{k}}^D(z,t)$, instead of Eq. (11), and following a procedure similar to that described in Appendix A, we are left with amplitude equations identical to Eq. (16), although with different coefficients. It is obvious that coefficients of the quadratic and cubic terms do not depend on Ma. It can also be shown that the coefficient of the linear term is the first term of the Taylor expansion of $\sigma_k(\mathrm{Ma})$ around $\mathrm{Ma}=\mathrm{Ma}_k$, i.e.,

$$\sigma_k^0=\frac{k(\mathrm{Ma}-\mathrm{Ma}_k)}{4(2k+\mathrm{Bi})} \ , \quad (17)$$

where a superscript 0 will denote a value of a coefficient computed by using neutral stability functions. Note that Eq. (17) is an insufficient approximation for low Biot numbers. As an indication, the mode $k=0$ is found to be amplified for $\mathrm{Bi}=0$ and $\mathrm{Ma}>0$ (which differs from the exact behavior of the growth constant, as seen in Fig. 2).

From Eqs. (9) and (11), it is seen that a roll mode with wave vector $\vec{k}_0$ is described by $A_{\vec{k}}=a_1(t)\delta(\vec{k}-\vec{k}_0)+\bar{a}_1(t)\delta(\vec{k}+\vec{k}_0)$, where δ is the Dirac delta function and an overbar denotes the complex conjugate. Substituting into (16) leads to the Ginzburg-Landau equation

$$\frac{\partial a_1}{\partial t}=\sigma_{k_0}^0 a_1+(2Z_{111}^0+Z_{-111}^0)a_1|a_1|^2 \ , \quad (18)$$

where Z_{111}^0 and Z_{-111}^0 stand for $Z_{\vec{k}_0\vec{k}_0\vec{k}_0}^0$ and $Z_{-\vec{k}_0\vec{k}_0\vec{k}_0}^0$, respectively. Defining a reduced distance to the threshold by

$$\epsilon=(\mathrm{Ma}-\mathrm{Ma}_{k_0})/\mathrm{Ma}_{k_0} \quad (19)$$

it is seen that at $\epsilon=0$, the rest state $a_1=0$ undergoes a pitchfork bifurcation to the steady amplitude

$$|a_{1s}|=\left[\frac{32(\mathrm{Bi}+3k_0)}{(\mathrm{Bi}+k_0)(39\,\mathrm{Bi}^2+248\,\mathrm{Bi}k_0+353k_0^2)}\epsilon\right]^{1/2} \quad (20)$$

obtained after evaluation of the cubic coefficients (see details in Appendix C).

Although strictly valid near the threshold, the limitations of this weakly nonlinear model for large ϵ are well known. Consider, for example, the temperature perturbation averaged in the horizontal direction (i.e., its $k=0$ Fourier component)

$$\langle T\rangle=T_{k=0}^D(z)=2|a_1|^2T_{01}^D(z)=O(\epsilon) \ , \quad (21)$$

where $T_{01}^D(z)$ is the only nonzero component of $U_{01}^D(z)$ (Appendix C). The total averaged temperature profile is obtained by adding the reference profile $-z$ to (21) and is represented in Fig. 3 for several values of ϵ. It is seen that in a region of depth $O(1/k_0)$ below the interface, the temperature profile is distorted (and somewhat homogenized) by Marangoni convection. It is also seen that unrealistic temperature distributions (strongly negative values of the mean temperature, leading to large unrealistic cold spots in steady regimes) are obtained for ϵ superior to about 1.5. Defining Δ as the bulk temperature de-

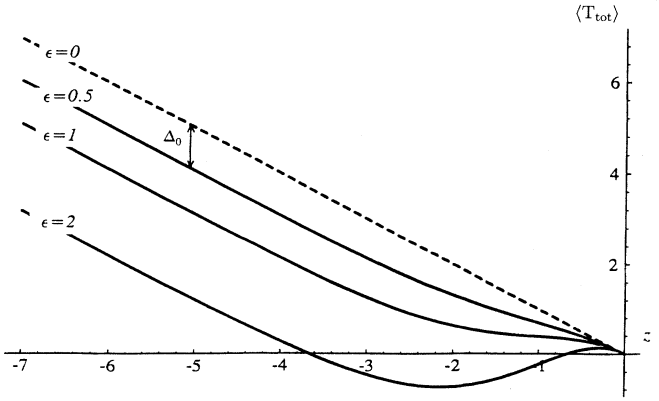

FIG. 3. Total temperature $\langle T_{\rm tot} \rangle$ averaged in the horizontal plane as a function of the vertical coordinate z, as computed from weakly nonlinear results, and for different values of $\epsilon=({\rm Ma}-{\rm Ma}_c)/{\rm Ma}_c$. The Biot number is ${\rm Bi}=0$ and the basic wave number is $k_0=1$. The distortion of the averaged temperature profile in the convective region near the interface $z=0$ creates a decrease Δ_0 of the bulk temperature with respect to the purely conductive value (dotted line, $\epsilon=0$). Δ_0 is here defined for $\epsilon=0.5$.

crease with respect to its value of the conductive rest state, we may compute that

$$\Delta^0=-2|a_{1s}|^2 \lim_{z\to-\infty} T_{01}^D(z) = \frac{32({\rm Bi}+3k_0)(5\,{\rm Bi}+7k_0)}{k_0(39\,{\rm Bi}^2+248k_0{\rm Bi}+353k_0^2)}\epsilon\,, \tag{22}$$

where the superscript 0 again denotes the weakly nonlinear result. The result (22) of course diverges for $\epsilon\to\infty$.

The importance of obtaining a better approximation of the bulk temperature decrease Δ is justified by the fact that it can be considered as equivalent to the classical Nusselt number Nu (more exactly to ${\rm Nu}-1$, which is also quadratic in the amplitudes). Indeed, for systems in which the temperature difference is kept constant (such as Rayleigh-Bénard convection between conduction boundaries), Nu is defined as the dimensionless ratio of the total to the conductive heat flux and therefore is a measure of the increase of the heat flux due to convection. For systems where the heat flux is kept constant (as in the present work), the decrease of the temperature difference between bulk and interface may also be perceived as an increase of the apparent thermal conductivity of the system due to Marangoni-Bénard convection. In the following sections it is shown that by using eigenvectors (12) instead of neutral stability functions a more realistic description of convective fields for large Ma can be obtained, together with interesting power laws for the variation of convective quantities in the limit ${\rm Ma}\to\infty$.

III. NUMERICAL RESULTS AND PHYSICAL INTERPRETATIONS

In this section we present results obtained by direct numerical integration of the set (16) for a two-dimensional domain of lateral length $L=2\pi/k_0$ with periodic boundary conditions. The amplitude of the Fourier modes is given by

$$A_{\vec{k}}(t)=\sum_{n=-N,n\neq0}^{+N} a_n(t)\delta(\vec{k}-n\vec{k}_0) \tag{23}$$

with $\bar{a}_n(t)=a_{-n}(t)$ and N sufficiently large to ensure numerical convergence. Substituting (23) in relation (16) leads to

$$\frac{\partial a_m}{\partial t}=\sigma_m a_m+\sum_p Z_{p,m}a_p a_{m-p}+\sum_{p,q} Z_{p,q,m}a_p a_q a_{m-p-q}\,, \tag{24}$$

where σ_m stands for σ_{mk_0}, $Z_{p,m}$ for $Z_{p\vec{k}_0,m\vec{k}_0}$, and $Z_{p,q,m}$ for $Z_{p\vec{k}_0,q\vec{k}_0,m\vec{k}_0}$, which are calculated as a function of the Marangoni number Ma.

In the following, we will take advantage of the fact that the length scale d of the problem is still arbitrary. We may thus choose $k_0=1$, which means that the dimensional length of the periodic box is $2\pi d$. From Eq. (14), the critical Marangoni number is given by ${\rm Ma}_c={\rm Ma}_{k=1}=8(1+{\rm Bi})$.

The system of equations (24) has been integrated for a wide range of Marangoni and Biot numbers. Despite the large number of unstable modes in some cases (increasing with Ma) and the presence of resonant quadratic terms (which are generally responsible for complicated phase coupling effects [29,30]), the long-term behavior appears to be surprisingly simple: a steady state is always reached, which is strongly dominated by the fundamental mode $n=1$. Since the number of modes N needed to ensure convergence is increasing with Ma (see Fig. 2), computer resources limited our investigations to Marangoni numbers of about ${\rm Ma}=500$ (for ${\rm Bi}=0$ and $N=20$).

We have also considered a simplified version of the system (24), which allows us to simulate the evolution of a larger number of amplitudes. This model is obtained by setting all cubic coefficients $Z_{p,q,m}$ with $p\neq m$ equal to zero. We then obtain

$$\frac{\partial a_m}{\partial t}=\left[\sigma_m-\sum_{q=1}^{N} S_{m,q}|a_q|^2\right]a_m+\sum_p Z_{p,m}a_p a_{m-p} \tag{25}$$

with $S_{m,q}=-2Z_{m,q,m}$. From Eq. (25), this quantity is seen to represent the strength with which the presence of the mode q lowers the effective growth rate of the mode m. The physical mechanism responsible for this stabilizing effect consists in the distortion of the mean temperature profile by convection (see Fig. 3), which lowers the destabilizing temperature gradient. A comparison of the time evolution and of the steady state values predicted by the full system (24) and the reduced set (25) reveals that the results differ only slightly (by less than 10% on the value of typical convective quantities at steady state, as shown in Fig. 6). In view of this rather good concordance, the mean temperature profile distortion by convection may be considered as a dominating effect in the nonlinear competition between unstable modes. Implications for wavelength selection between fastest growing

and critical modes are discussed later on in this section.

Since it is legitimate to admit that the simplified system (25), which can be considered as a "mean-field" [32] version of the problem, is useful for simulating the interactions of a larger number of modes (up to $N=75$), larger Marangoni number values can also be investigated. Again, even for Marangoni numbers as large as 4000 (for Bi=0, i.e., $\epsilon \simeq 500$), the long-term behavior is not modified, independently of the initial conditions (here selected as a numerical "white noise," i.e., randomly chosen complex amplitudes of magnitude 10^{-8}–10^{-3}): the final state is still steady and dominated by the fundamental mode.

A sequence of a typical transient simulation is represented in Fig. 4. For sufficiently small initial perturbations, a convective structure dominated by the fastest linearly growing mode (the mode closest to $k_{\max}$) is observed after a relatively short time. This is the case as long as nonlinear effects can be neglected. At higher time intervals, this $k_{\max}$ structure is progressively replaced by larger and larger wavelength structures via a complex process of coalescence of neighboring convective cells. This evolution finally tends to the steady state with two convective cells (one period) occupying the entire domain, as expected (fundamental mode). The properties of this steady state will be investigated in Sec. IV.

It is interest to compare Fig. 4 with the experimental observations made by Linde, Schwartz, and Wilke [5] in mass transfer systems. Note that these systems might actually correspond to high values of Bi since the diffusion coefficients are generally much larger in the gas than in the liquid phase. However, our simulations were not found to be strongly dependent on Bi for large Ma. Linde, Schwartz, and Wilke interpreted the observed growth of the mean wavelength of the convective pattern as an effect due to the nonstationary mass transfer occurring in their experiments. Indeed, after that the experiment is started by putting in contact a gas phase containing a surface active solute with the liquid phase; the diffusion of this solute through the interface creates a growing diffusive boundary layer, which induces convective motions in the liquid, with a wavelength that scales with the thickness of this boundary layer.

Since a natural length scale such as this boundary layer thickness is absent in our formulation, the wavelength selection observed in Fig. 4 has to be intrinsically related to the nonlinear mechanism of heat (or mass) convective transport. This effect was indeed shown (see Fig. 3) to

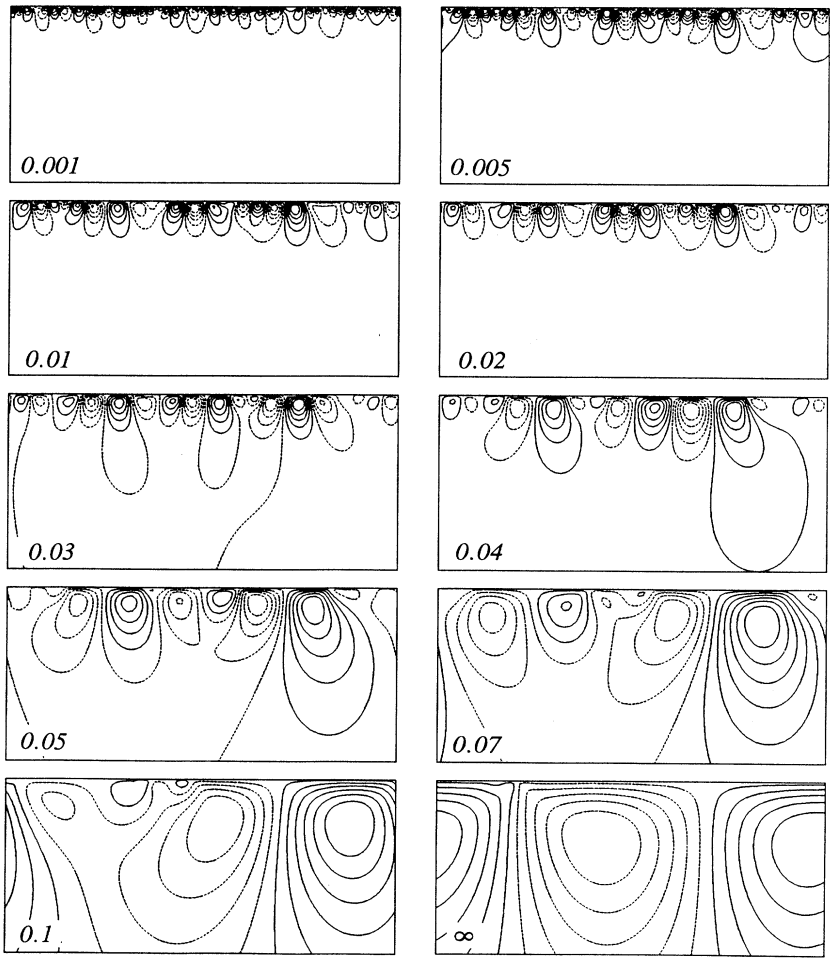

FIG. 4. Evolution of the stream function pattern for Ma=3000 ($\epsilon=374$), Bi=0, and $N=75$. Solid closed curves correspond to clockwise motion. The initial condition was selected as a random noise of amplitude 10^{-5}. The stream function is rescaled at each snapshot (the reduced time is indicated). The fastest growing perturbation is dominating for times $t<0.03$. A continuous growth of the mean wavelength of the pattern is observed, the later stages of which tend to a steady state with two convective cells (one period) in the simulation domain, after a time of order unity (in units $L^2/4\pi^2\kappa$, where L is the horizontal period).

create a homogenization of the temperature (or concentration) profile in a convective region located below the interface. This is also apparent in Fig. 5, which represents the temperature profile averaged along the horizontal direction corresponding to the evolution depicted in Fig. 4. It is seen that the temperature uniformization due to convection is more important at large times, when the penetration depth is large. The growth mechanism can be explained by the following considerations. Suppose that at one particular instant, the convective structure has a given mean wavelength λ. Since the convective cells have to preserve a certain height-to-width ratio, temperature is practically homogenized in a region of depth λ below the interface. Modes with wavelengths smaller than λ may be considered as stable since they experience a nearly isothermal environment. On the contrary, modes with wavelengths larger than λ can penetrate deeply enough into the bulk of the liquid and bring hot fluid from the still conductive zone to the interface. The effective growth rate of these modes remains nearly unchanged by the convective structure so that these modes continue to grow (but slower and slower due to their growing inertia) and tend to replace smaller wavelength structures. The pattern wavelength λ may thus be expected to grow indefinitely, at least in an infinite system. In real experiments, the final wavelength will probably be determined by the actual depth of the experimental container (thus near the critical wavelength), indicating that an intrinsic wavelength is likely to be inexistent for the pure Marangoni-Bénard problem. Note that from the point of view of wavelength selection, the evolution described above presents some similarities with coarsening processes observed during spinodal decomposition phenomena in binary mixtures [36].

A last remark about Fig. 5 concerns the temperature profile near the interface. Since the vertical velocity is vanishing at the interface, some kind of thermal boundary layer is created there, in which the temperature gradient quickly recovers its bulk value. In Rayleigh-Bénard convection, boundary layer effects are known to play a decisive role in the mechanisms of transition to turbulence (especially for high Prandtl number fluids [20]). However, despite the very high values of the Marangoni number, boundary layer instabilities have not been observed in our simulations, probably due to the different nature of these boundary layers (in particular the absence of the no-slip condition for Marangoni-Bénard problems). Furthermore, it cannot be rejected that this kind of phenomenon could appear for larger driving forces than those investigated in this work (up to Ma=4000).

Finally, let us mention that a direct comparison of the results obtained from the present model (amplitude equations limited to third order) with a finite-difference resolution of the governing equations is in progress and will

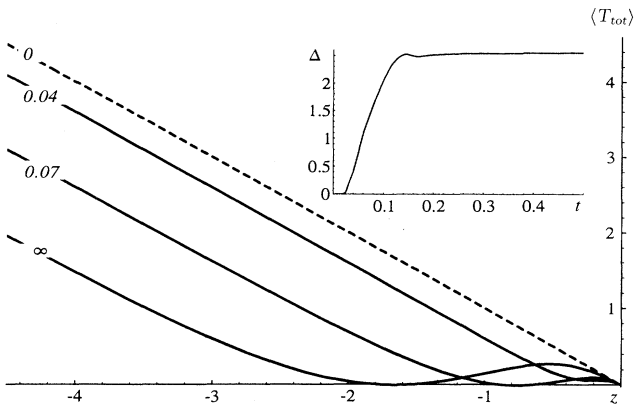

FIG. 5. Evolution of the total temperature $\langle T_{\rm tot} \rangle$ averaged in the horizontal plane as a function of the vertical coordinate z. The Biot number is Bi=0. Several times are considered, which correspond to the simulation depicted in Fig. 4. A homogenization of the temperature in a domain whose depth is growing with time occurs, which results in growth of the bulk temperature decrease Δ with time (see inset).

be reported elsewhere. Preliminary results exhibit a satisfactory agreement concerning the qualitative evolution of the system (i.e., the growth of the mean wavelength up to the final steady state with the largest wavelength). This confirms that the most important ingredient responsible for this process is indeed the mean temperature profile distortion by convection. This in turn indicates that mean-field approximations [32], neglecting all nonlinear effects except the change of the mean temperature profile owing to the convective heat transport, can lead to satisfactory approximations of highly supercritical behaviors.

IV. ANALYSIS OF STEADY STATES

A. Bifurcation of rolls

Since the steady state reached by both full (24) and reduced (25) models is strongly dominated by the fundamental mode $n=1$, we seek an approximate solution by setting to zero all harmonics a_n with $n>1$. The set (25) then reduces to the single equation

$$\frac{\partial a_1}{\partial t} = [\sigma - S_{11}|a_1|^2]a_1 \tag{26}$$

describing a pitchfork bifurcation similar to Eq. (18) but where the coefficients are now computed from the eigenfunctions U_k^σ and thus depend on Ma. After computation of these coefficients, the steady convective solution of (26) is finally found as

$$|a_1|^2 = \frac{\sigma}{S_{11}} = \frac{(\mathrm{Ma}-\mathrm{Ma}_c)\sigma^2(3+\sqrt{1+\sigma})^3}{(1+\mathrm{Bi})^2[512(\mathrm{Ma}+\sigma^2)+\mathrm{Ma}(3\sigma-8)(3+\sqrt{1+\sigma})^3]}\ , \tag{27}$$

where the growth rate σ is solution of the dispersion relation (13) and thus also depends on Ma. According to Eq. (26),

where the growth rate σ is solution of the dispersion relation (13) and thus also depends on Ma. According to Eq. (26), the solution (27) is stable provided $\sigma>0$ ($S_{11}>0$) which is equivalent to $\mathrm{Ma}>\mathrm{Ma}_c=8(1+\mathrm{Bi})$ (we have set $k_0=1$).

$$\Delta=\frac{8(\mathrm{Ma}-\mathrm{Ma}_c)(3+\sqrt{1+\sigma})^3\left[\sigma-2+\dfrac{8(\mathrm{Ma}+\sigma^2)}{\mathrm{Ma}(1+\sqrt{1+\sigma})^2}\right]}{512(\mathrm{Ma}+\sigma^2)+\mathrm{Ma}(3\sigma-8)(3+\sqrt{1+\sigma})^3} . \tag{28}$$

This expression is represented in Fig. 6, together with results obtained from the integration of the full system (24) and of the reduced system (25). Another result found in Fig. 6 is the expression (22), which reduces to $\Delta^0=672\epsilon/353$ for $\mathrm{Bi}=0$ and $k_0=1$. Clearly, this result is only valid near the threshold. At the contrary, the expression (28) for Δ leads to the result $\Delta=14/5\epsilon$ near the threshold [which is overestimated due to the negligence of the stabilizing coefficient Z_{-111}; see Eq. (18)]. Nevertheless, Eq. (28) appears to be a better approximation of the bulk temperature decrease for large Marangoni numbers (because Z_{-111} becomes negligible compared to Z_{111}). The corresponding mean temperature profile can also be shown to be more realistic since it does not exhibit cold spots such as those appearing in Fig. 3 but is rather close to Fig. 5. The behavior at an infinite Marangoni number is given at the end of this section.

B. Competition between hexagons and rolls

In view of the good agreement between the analytical result (28) and the results of the numerical integration of (24), we shall reexamine the problem of the competition between three sets of rolls forming angles of 60° with each other. We thus consider

$$\begin{aligned}A_{\vec{k}}=&a_1(t)\delta(\vec{k}-\vec{k}_1)+a_2(t)\delta(\vec{k}-\vec{k}_2)\\&+a_3(t)\delta(\vec{k}-\vec{k}_3)+\bar{a}_1(t)\delta(\vec{k}+\vec{k}_1)\\&+\bar{a}_2(t)\delta(\vec{k}+\vec{k}_2)+\bar{a}_3(t)\delta(\vec{k}+\vec{k}_3) ,\end{aligned} \tag{29}$$

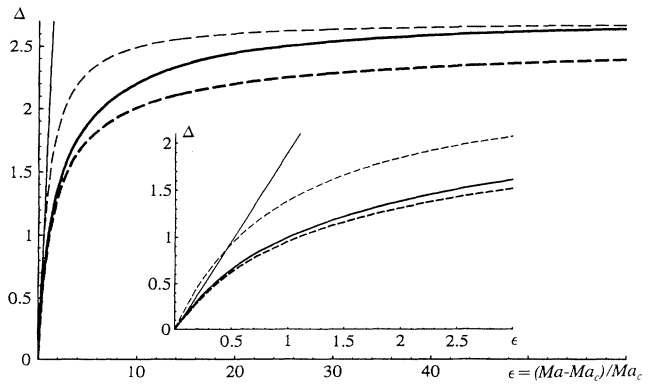

FIG. 6. Bulk temperature decrease Δ as a function of the distance to the threshold $\epsilon=(\mathrm{Ma}-\mathrm{Ma}_c)/\mathrm{Ma}_c$ for $\mathrm{Bi}=0$. Thick full curve, results of the numerical integration of the full system (24); thick dotted curve, numerical integration of the "mean-field" system (25); thin full line, the weakly nonlinear result $\Delta^0=672\epsilon/353$; thin dotted curve, the analytical result for Δ given by Eq. (28) of the text. The inset represents a zoom of a region near the origin.

where the ordering of unit vectors $\vec{k}_i$, $|i|=1,2,3$, is defined by Fig. 7. From Eq. (16), the corresponding amplitude equations are

$$\begin{aligned}\frac{\partial a_1}{\partial t}&=\sigma a_1+\delta a_2\bar{a}_3-[\alpha_1|a_1|^2+\alpha_2(|a_2|^2+|a_3|^2)]a_1 ,\\ \frac{\partial a_2}{\partial t}&=\sigma a_2+\delta a_1 a_3-[\alpha_1|a_2|^2+\alpha_2(|a_1|^2+|a_3|^2)]a_2 ,\\ \frac{\partial a_3}{\partial t}&=\sigma a_3+\delta\bar{a}_1 a_2-[\alpha_1|a_3|^2+\alpha_2(|a_1|^2+|a_2|^2)]a_3 ,\end{aligned} \tag{30}$$

where

$$\delta=2Z_{1,2} , \tag{31}$$

$$\alpha_1=-(2Z_{1,1,1}+Z_{-1,1,1}) , \tag{32}$$

$$\alpha_2=-2(Z_{1,1,1}+Z_{2,1,1}+Z_{-2,1,1}) , \tag{33}$$

and $Z_{p,q,r}$ stands for $Z_{\vec{k}_p,\vec{k}_q,\vec{k}_r}$ (symmetry considerations have been used to minimize the number of coefficients to be calculated).

The discussion of the gradient system (30) is well known [23–26,37]: writing $a_n=r_n\exp[i\varphi_n]$, we obtain the equation $\partial\varphi/\partial t=-\delta\sin\varphi(r_1^2r_3^2+r_2^2r_3^2+r_1^2r_2^2)/r_1r_2r_3$ (with $r_n\neq0$) for $\varphi=\varphi_2-\varphi_1-\varphi_3$, showing that $\varphi=0$ and π are the only possible stationary values of φ. Then it is found that qualitatively different fixed points of Eqs. (30) are (when $\alpha=\alpha_1+2\alpha_2>0$) the rest solution

$$r_1=r_2=r_3=0 , \tag{34}$$

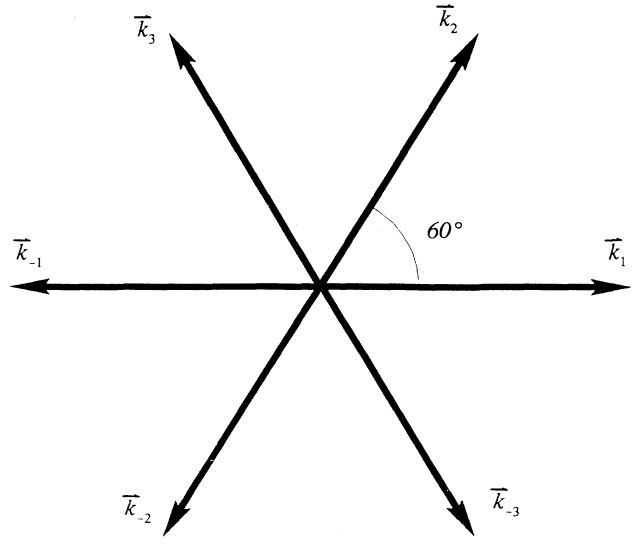

FIG. 7. Definition of the basic wave vectors for the study of the competition between rolls and hexagons ($|\vec{k}_i|=1$).

the roll solutions

$$r_2=r_3=0, \quad r_1=(\sigma/\alpha_1)^{1/2}, \tag{35}$$

the up-hexagon solutions

$$\varphi=0, \quad r_1=r_2=r_3=[\delta\pm(\delta^2+4\sigma\alpha)^{1/2}]/2\alpha, \tag{36}$$

and the down-hexagon solutions

$$\varphi=\pi, \quad r_1=r_2=r_3=[-\delta+(\delta^2+4\sigma\alpha)^{1/2}]/2\alpha. \tag{37}$$

The analytical form of the coefficients δ, α_1, and α_2 (depending on Ma) is not written down for conciseness. Rather, Fig. 8 presents their variation with the distance to the threshold ϵ for various Biot numbers. Bifurcation diagrams are represented in Figs. 9 and 10.

Figure 9 represents the bulk temperature decrease Δ as a function of the distance to the threshold ϵ for solutions (35)–(37). As expected, up hexagons (upflows at the center of the hexagons) are the only stable solutions just above the threshold and rolls become stable only at large ϵ. Down hexagons (downflow at the center) are always unstable because $\delta>0$ (which is different from the case of very low Prandtl number fluids [26]). Note that, although not apparent on the figure, the first bifurcation to up hexagons at $\epsilon=0$ is slightly hysteretic: the depth of this subcritical region is 3.3% (for Bi=0) in our model, slightly larger than the 2.3% value of Scanlon and Segel [14]. This is due to the fact that we have neglected the stabilizing action of "secondary" modes, i.e., those generated by quadratic interaction of the "primary" modes. This is done since it is natural to expect that these modes become unimportant for large Ma, as observed in the case of two-dimensional simulations, characterized by a strong domination of the fundamental mode $n=1$ (see Sec. III). When the amplitudes of these harmonics are included in Eq. (29) and finally eliminated using adiabatic slaving [25,26,28], the 2.3% value of the hysteresis is recovered. It is also possible to recover the result 0.56% of Bragard and Lebon [24] in the case of a layer of finite depth (the calculation of coefficients is then fully numerical). It is also apparent that the percentage depth of the subcritical region increases with the Biot number.

An interesting result of the present analysis is that at large Marangoni numbers, the stability properties are not qualitatively modified with respect to the results of Scanlon and Segel [14]: these authors predicted that rolls

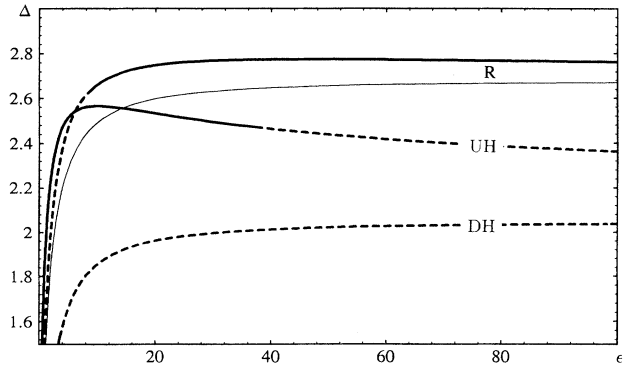

FIG. 9. Bulk temperature decrease Δ as a function of the distance to the threshold ϵ for Bi=0. *R*, rolls; UH, up hexagons; DH, down hexagons. Solid curves represent stable states, while dotted curves represent unstable states. The thin solid line represents the analytical result given by Eq. (28) of the text for the bulk temperature decrease of rolls.

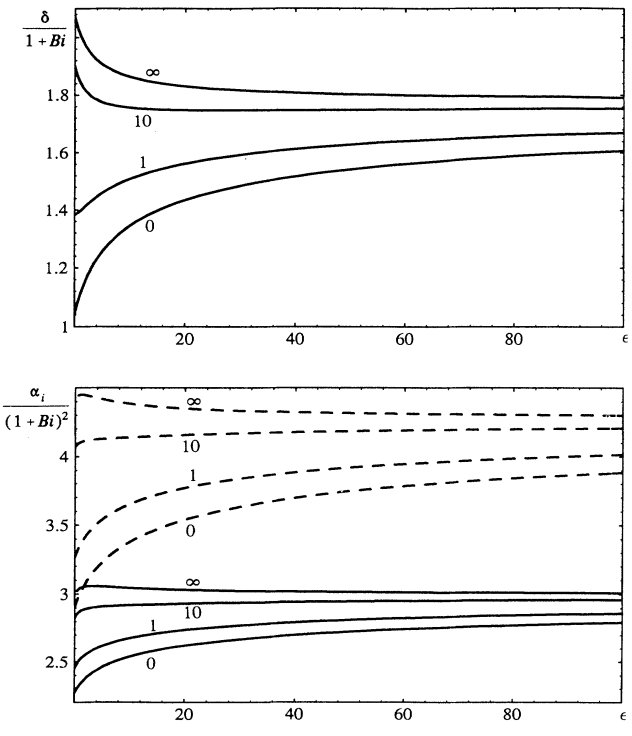

FIG. 8. Coefficients $\delta/(1+\mathrm{Bi})$ (upper graph), $\alpha_1/(1+\mathrm{Bi})^2$ (lower graph, solid curves), and $\alpha_2/(1+\mathrm{Bi})^2$ (lower graph, dashed curves) as a function of the distance to the threshold $\epsilon=[\mathrm{Ma}-\mathrm{Ma}_c(\mathrm{Bi})]/\mathrm{Ma}_c(\mathrm{Bi})$, for various Biot numbers Bi (indicated on each curve).

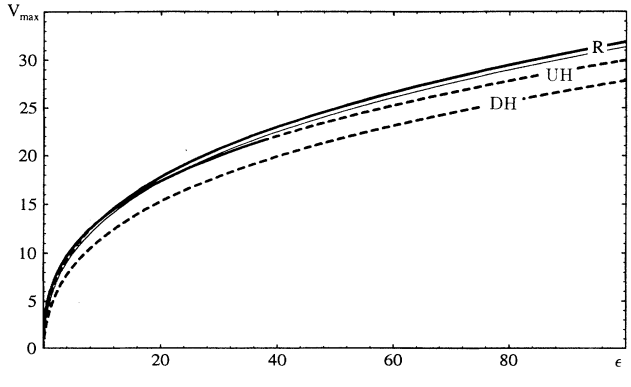

FIG. 10. Maximal surface velocity $V_{\max}$ as a function of the distance to the threshold ϵ for Bi=0. *R*, rolls; UH, up hexagons; DH, down hexagons. Solid curves represent stable states, while dotted curves correspond to unstable states. The thin solid line represents the analytical result for the maximal surface velocity of rolls.

should become stable above a value $\epsilon_1=64$ (our value is $\epsilon_1=8.6$) of the constraint, while up hexagons should become unstable above $\epsilon_2=196$ (our value is $\epsilon_2=37$). A bistability region (leading to hysteresis effect between rolls and hexagons) thus exists between ϵ_1 and ϵ_2. This qualitative concordance reinforces the idea that this hysteresis region could be a physical reality, although the domain of validity of the amplitude equations is not guaranteed for such large values of ϵ. Finally, we have represented the maximal surface velocity for the bifurcating solutions (35)–(37) in Fig. 10, showing that this quantity is not strongly dependent on the particular planform selected.

C. Asymptotic behaviors for $\mathrm{Ma}\to\infty$

It results from the examination of the previous figures that the asymptotic behaviors of the relevant convective quantities for $\mathrm{Ma}\to\infty$ obey different power laws than those generally derived near the threshold by using classical perturbation methods. In particular, a saturation is observed for the bulk temperature decrease Δ (which, as mentioned earlier, can be considered as equivalent to the Nusselt number). The purpose of the following calculations is to derive asymptotic results for Δ, for the maximal surface velocity $V_{\max}$, as well as for the surface temperature deviation ΔT_{surf}, which we define as the difference between maxima and minima of temperature on the free surface.

From the dispersion relation (13), it is straightforward that

$$\sigma_k \to \left[\frac{k\,\mathrm{Ma}}{2}\right]^{2/3} \quad \text{for } \mathrm{Ma}\to\infty \ . \tag{38}$$

The asymptotic value of the amplitude of rolls is derived from Eq. (27),

$$|a_1|^{\mathrm{rolls}} \to \frac{\mathrm{Ma}^{1/3}}{2^{1/3}3^{1/2}(1+\mathrm{Bi})} \tag{39}$$

and it is calculated from Eq. (28) that the saturation value of the bulk temperature decreases for a roll structure is

$$\Delta^{\mathrm{rolls}} \to \tfrac{8}{3} \simeq 2.66 \tag{40}$$

independently of the value of the Biot number. This result is confirmed by all the curves of Fig. 6.

It is readily computed that the maximal surface velocity is

$$V_{\max}^{\mathrm{rolls}} \to \frac{8\,\mathrm{Ma}^{1/3}}{2^{1/3}3^{1/2}} \simeq 3.67\ \mathrm{Ma}^{1/3} \ , \tag{41}$$

while the amplitude of the surface temperature variations is given by

$$\Delta T_{\mathrm{surf}}^{\mathrm{rolls}} \to \frac{32\,\mathrm{Ma}^{-2/3}}{2^{1/3}3^{1/2}} \simeq 14.66\ \mathrm{Ma}^{-2/3} \ . \tag{42}$$

The corresponding expressions for hexagons (although unstable with respect to roll disturbances for $\mathrm{Ma}\to\infty$) can also be derived analytically. We obtain

$$\delta \to \tfrac{16}{9}(1+\mathrm{Bi}) \ , \tag{43}$$

$$\alpha_1 \to 3(1+\mathrm{Bi})^2 \ , \tag{44}$$

$$\alpha=\alpha_1+2\alpha_2 \to \frac{(104\,733\,031-60\,445\,052\sqrt{3})}{243(7+4\sqrt{3})}(1+\mathrm{Bi})^2 \simeq 11.56(1+\mathrm{Bi})^2 \ . \tag{45}$$

It follows that

$$\Delta^{\mathrm{hexagons}} \to 2.08 \tag{46}$$

for the bulk temperature decrease of hexagons [both up and down hexagons lead to the same value for $\mathrm{Ma}\to\infty$, as seen from Eqs. (36) and (37) and in Fig. 9]. This value is inferior to the value $\frac{8}{3}$ of rolls. However, this should not be taken as a rigorous justification for the instability of hexagons since it is well known that the principle of maximization of the convective heat transport, originally proposed by Malkus [31], does not lead to stability predictions that are generally valid [32].

Finally, the maximal surface velocity tends to

$$V_{\max}^{\mathrm{hexagons}} \to 3.29\ \mathrm{Ma}^{1/3} \tag{47}$$

and the amplitude of the surface temperature deviations is

$$\Delta T_{\mathrm{surf}}^{\mathrm{hexagons}} \to 16.81\,\mathrm{Ma}^{-2/3} \ . \tag{48}$$

To check the assumptions used in our analysis, it should be interesting to compare the above results with a full numerical integration of the problem. Preliminary finite-difference simulations indicate a slow growth of the bulk temperature decrease, as well as an increase of the velocities (although with an exponent larger than 1/3) coexistent with a slow decrease of the surface temperature variations. This allows us to place some confidence in our analysis. In particular, the exponents 1/3 and $-2/3$ may be considered as first approximations that could be refined by deriving higher-order contributions to the amplitude equations. It appears also that the present asymptotic analysis leads to results that are difficult to check by finite-difference simulations. Indeed, since convergence of results may only be expected for very high values of the Marangoni number, numerical difficulties are encountered, mainly due to the presence of very steep surface temperature gradients at the cold points, where the fluid moves downwards.

We conclude this section by remarking about an important mathematical aspect of the pure Marangoni-Bénard instability. A particular feature of this problem is that the neutral stability condition provides Ma as a single-valued function of the wave number k. This means that above the corresponding critical value, one and only one eigenmode is unstable, as large as Ma can be. This has to be contrasted [33] with Rayleigh-Bénard instabilities, where n eigenmodes are linearly unstable above the value $\mathrm{Ra}_n=(k^2+n^2\pi^2)^3/k^2$ of the Rayleigh number (pure Rayleigh-Bénard convection between stress-free boundaries). Clearly, the above analysis would require nontrivial modifications to account for interactions between these unstable vertical modes. Physically, this difference between Marangoni-Bénard and Rayleigh-Bénard problems is certainly related to the different na-

tures of the surface and the bulk forces. This could also explain why neither boundary layer instabilities nor subsequent transitions to turbulence have been observed in our model, in the range of Marangoni numbers investigated.

V. CONCLUSIONS

Pure thermocapillary instability in layers with nondeformable interface and infinite Prandtl number has been studied. The model is based on the assumptions that the dynamics is determined by the interactions of the unstable eigenmodes of the linear stability problem and that the evolution equations describing their interactions can be limited to third order in their amplitudes. Although strictly valid near the threshold, this model has to be considered as an approximation (similar to a truncated modified Galerkin method) far from it. Attention has been restricted to short-wavelength effects, so that the layer has been assumed infinitely deep.

The first part of the analysis has focused on the two-dimensional wavelength selection problem at moderately large Marangoni numbers, for which the wavelength of the fastest growing disturbance is much smaller than the critical wavelength. The transient numerical integration of third-order amplitude equations has shown that, although a structure dominated by the fastest growing disturbance can appear at a given instant, it is progressively replaced by longer-wavelength structures. A steady state is always reached, whose wavelength is equal to the size of the (periodic) simulation domain. This is confirmed by a finite-difference integration of the problem. Although the fastest growing wavelength is a finite quantity, it appears that the Marangoni-Bénard instability cannot induce stable localized structures with intrinsic wavelengths independent of the experiment dimensions (at least up to Ma=4000). The physical mechanism responsible for this convective cells growth process is shown to be related to the nonlinear convective heat transport, which creates a distortion of the temperature field in the region located near the free surface. The distortion of the horizontally averaged temperature profile (the cause of the instability) has a stabilizing effect on short-wavelength modes, but leaves the growth rate of long-wavelength structures relatively unchanged. This produces a growth of the pattern wavelength, which presents some resemblance with experimental results of Linde, Schwartz, and Wilke [5], although we have not studied this point in details since transient evolution of the diffusive (boundary layer) profile is not taken into account in our analysis.

Properties of the steady states observed in the convective system have been investigated for both rolls and hexagonal structures. Contrary to existing weakly nonlinear theories, our method (differing by the use of eigenfunctions rather than neutral stability functions) appears to lead to physically realistic results, at least qualitatively, for very large Marangoni numbers. This is conjectured from examination of the behavior of some relevant convective quantities. The decrease of the bulk temperature due to Marangoni convection has been found to present a saturation when the Marangoni number is increased (while the weakly nonlinear result is a linear growth). The velocities are found to grow as $\mathrm{Ma}^{1/3}$ as $\mathrm{Ma}\to\infty$, while the surface temperature variations decrease as $\mathrm{Ma}^{-2/3}$. However, due to the assumptions underlying our model, these behaviors should be considered as first approximations that could be refined by including higher-order interactions in the amplitude equations.

The analysis of the competition between rolls and hexagons confirms earlier results [14,23–26], quantitatively (near threshold) and qualitatively (far from threshold). At small Marangoni numbers, up hexagons are the only stable solutions (the first bifurcation is slightly hysteretic), while rolls are the only stable solutions at very large Marangoni numbers. Down hexagons are always unstable ($\mathrm{Pr}\to\infty$). The transition between up hexagons and rolls is found to be hysteretic, as in other problems (see, e.g., [34]). However, this transition has been found to occur for lower Marangoni numbers than in [14] and with a smaller hysteresis loop.

ACKNOWLEDGMENTS

P.C. acknowledges financial support from the European Office of Aerospace Research and Development, for allowing his stay in Case Western Reserve University, during which part of this work was achieved. We are grateful to Professor S. Ostrach, Professor Y. Kamotani, and their team for welcoming P.C. in the department. P.C. would also like to thank Professor F. McCaughan and K. McDuffy from Case Western Reserve University and R. Skarda from NASA Lewis for comments, access to computers, and hospitality. It is a pleasure for us to thank Professor A. Nepomnyashchy from the Centre for Research in Nonlinear Phenomena (Technion, Haifa) for beneficial discussions and Professor G. Gershuni from Perm State University. We finally thank Ph. Géoris for finite-difference simulations and discussions. This research has been supported by the Belgian program on InterUniversity Poles of Attraction (PAI 21) initiated by the Belgian State, Federal Services of Scientific, Technical and Cultural Affairs. The scientific responsibility is assumed by its authors.

APPENDIX A: DERIVATION OF AMPLITUDE EQUATIONS

Using Eq. (11), we may write Eq. (10) as a differential problem for $U_k^D(z,t)$:

$$\mathcal{L}_{\vec{k}}(U_k^D)-\mathrm{Ma}M_{\vec{k}}(U_k^D)=-A_{\vec{k}}[\mathcal{L}_{\vec{k}}(U_k^a)-\mathrm{Ma}M_{\vec{k}}(U_k^a)]+\frac{\partial A_{\vec{k}}}{\partial t}\Theta_{\vec{k}}(U_k^a)+\int d\vec{k}'\,A_{\vec{k}'}A_{\vec{k}-\vec{k}'}N_{\vec{k}',\vec{k}-\vec{k}'}(U_{k'}^a,U_{k-k'}^a)$$
$$+\int d\vec{k}'N_{\vec{k}',\vec{k}-\vec{k}'}(U_{k'}^D,U_{k-k'}^D)+\int d\vec{k}'\,A_{\vec{k}'}[N_{\vec{k}',\vec{k}-\vec{k}'}(U_{k'}^a,U_{k-k'}^D)+N_{\vec{k}-\vec{k}',\vec{k}'}(U_{k-k'}^D,U_{k'}^a)] \quad \text{(A1)}$$

where the time-derivative of U_k^D has been canceled as a result of our assumption to neglect the dynamics of the damped modes (the slaving principle). Note that because of Eq. (11), the boundary conditions can only be satisfied if U_k^D belongs to E. A very rough (and insufficient) model could be obtained at this stage by projection of Eq. (A1) onto some functions (generally the adjoint functions [35]) and assuming $U_k^D=0$. We would then obtain an equation of the form (16), but without stabilizing cubic terms. Rather, we will try to solve (A1) for U_k^D. This can be done only if (A1) is compatible, which is not the case at $\mathrm{Ma}=\mathrm{Ma}_k$ (the kernel of the left-hand side operator is then not empty), except if the second member is orthogonal to the solution of the adjoint neutral stability problem (Fredholm's condition). This leads to the amplitude equations

$$\frac{\partial A_{\vec{k}}}{\partial t}=\sigma_k A_{\vec{k}}+\int d\vec{k}' Z_{\vec{k}'\vec{k}} A_{\vec{k}'} A_{\vec{k}-\vec{k}'} - \int d\vec{k}' A_{\vec{k}'} \frac{\langle V_k^*, N_{\vec{k}',\vec{k}-\vec{k}'}(U_{k'}^a, U_{k-k'}^D)\rangle}{\tau_k} , \quad \text{(A2)}$$

where Eq. (12) has been used and it has been anticipated that the velocity (and pressure) components of U_k^D are zero. This will become apparent later and is a consequence of the linearity of the equations of motion. In (A2), $\langle V_k^*, \rangle$ denotes the projection on the adjoint neutral stability solution (derived in Appendix B), $\tau_k=\langle V_k^*, \Theta_{\vec{k}}(U_k^a)\rangle$ is the normalization factor, and the quadratic coefficients are given by

$$Z_{\vec{k}'\vec{k}}=-\frac{\langle V_k^*, N_{\vec{k}',\vec{k}-\vec{k}'}(U_{k'}^a, U_{k-k'}^a)\rangle}{\tau_k} . \quad \text{(A3)}$$

Now, by inserting the projected part (A2) into the complete equation (A1), we obtain

$$\mathcal{L}_{\vec{k}}(U_k^D)-\mathrm{Ma}M_{\vec{k}}(U_k^D) = \int d\vec{k}' A_{\vec{k}'} A_{\vec{k}-\vec{k}'} N^{\mathrm{NR}}_{\vec{k}',\vec{k}-\vec{k}'}(U_{k'}^a, U_{k-k'}^a) + \int d\vec{k}' A_{\vec{k}'} N^{\mathrm{NR}}_{\vec{k}',\vec{k}-\vec{k}'}(U_{k'}^a, U_{k-k'}^D) , \quad \text{(A4)}$$

where the nonresonant part of a term X is defined by $X^{\mathrm{NR}}=X-\tau_k^{-1}\langle V_k^*, X\rangle\Theta_{\vec{k}}(U_k^a)$, such that $\langle V_k^*, X^{\mathrm{NR}}\rangle=0$ for every X. This ensures that (A4) is compatible for every Ma. Now, the form of Eq. (A4) suggests an iterative series solution, starting with

$$U_k^D=\int d\vec{k}' A_{\vec{k}'} A_{\vec{k}-\vec{k}'} U^D_{kk'} \quad \text{(A5)}$$

in which $U^D_{kk'}$ is obtained from

$$(\mathcal{L}_{\vec{k}}-\mathrm{Ma}M_{\vec{k}})U^D_{kk'}=N^{\mathrm{NR}}_{\vec{k}',\vec{k}-\vec{k}'}(U_{k'}^a, U_{k-k'}^a) . \quad \text{(A6)}$$

Substituting this result in the right-hand side of (A4) leads to higher-order corrections [cubic terms for U_k^D, generating quartic and higher-order terms in (A2), which are not considered in our model]. We limit the calculation of U_k^D to (A5) and (A6) such that the compatibility equations (A2) reduce to the amplitude equations (16), with quadratic coefficients given by (A3) and cubic coefficients given by

$$Z_{\vec{k}'\vec{k}''\vec{k}}=-\frac{\langle V_k^*, N_{\vec{k}',\vec{k}-\vec{k}'}(U_{k'}^a, U^D_{k-k',\vec{k}''})\rangle}{\tau_k} . \quad \text{(A7)}$$

APPENDIX B: SOLUTION OF THE LINEAR PROBLEM

Starting from Eq. (12), the neutral stability problem ($\sigma_k=0$) can be written as

$$S_{\vec{k}}(U_k^0)=\mathcal{L}_{\vec{k}}(U_k^0)-\mathrm{Ma}_k M_{\vec{k}}(U_k^0) = \begin{bmatrix} (D^2-k^2)\vec{V}^0_{rk}-i\vec{k}p_k^0 \\ (D^2-k^2)W_k^0-Dp_k^0 \\ DW_k^0+i\vec{k}\cdot\vec{V}^0_{rk} \\ (D^2-k^2)T_k^0+W_k^0 \\ [D\vec{V}^0_{rk}+i\vec{k}\,\mathrm{Ma}_k T_k^0]_{z=0} \end{bmatrix} . \quad \text{(B1)}$$

The solution of this problem that belongs to E [i.e., which satisfies boundary conditions (2) and (3)] reads

$$U_k^0=\begin{bmatrix} \vec{V}^0_{rk} \\ W_k^0 \\ p_k^0 \\ T_k^0 \end{bmatrix} = e^{kz}\begin{bmatrix} -4i\vec{k}(k+\mathrm{Bi})(1+kz) \\ -4k^2(k+\mathrm{Bi})z \\ -8k^2(k+\mathrm{Bi}) \\ 1-(k+\mathrm{Bi})z+k(k+\mathrm{Bi})z^2 \end{bmatrix} , \quad \text{(B2)}$$

where $k=|\vec{k}|$, and the normalization condition has been chosen such that $T_k^0(z=0)=1$. The compatibility condition leads to the neutral stability relation $\mathrm{Ma}_k=8k(k+\mathrm{Bi})$. We can now define adjoint vectors

$$V^*=\begin{bmatrix} \vec{V}_r^* \\ W^* \\ p^* \\ T^* \\ \vec{X}^* \end{bmatrix} \quad \text{(B3)}$$

belonging to a set E^* of adjoint boundary conditions to be defined later on.

A scalar product is introduced in the usual way (see, e.g., [14,24]) by

$$\langle V^*, S_{\vec{k}}(U)\rangle=\int_{-\infty}^0 [\overline{\vec{V}_r^*}\cdot\vec{S}_1+\overline{W^*}S_2+\overline{p^*}S_3+\overline{T^*}S_4]dz + [\overline{\vec{X}^*}\cdot\vec{S}_5]_{z=0} , \quad \text{(B4)}$$

where S_i, $i=1,\ldots,5$, are the components of (B1) and the overbar denotes the complex conjugate. We also define the adjoint operator S_k^* of $S_{\vec{k}}$ by

$$\langle V^*, S_{\vec{k}}(U)\rangle=\langle S_k^*(V^*), U\rangle \quad \text{(B5)}$$

for all U belonging to E and V^* to E^*. Integration by parts leads to

$$S_k^*(V^*)=\begin{bmatrix}(D^2-k^2)\vec{V}_r^*-i\vec{k}p^*\\(D^2-k^2)W^*-Dp^*+T^*\\DW^*+i\vec{k}\cdot\vec{V}_r^*\\(D^2-k^2)T^*\end{bmatrix} \tag{B6}$$

and the cancellation of the boundary term gives E^* as the set of sufficiently derivable functions satisfying

$$\vec{V}_r^*, W^*, DT^*, p^* \to 0 \quad \text{for } z\to-\infty\ , \tag{B7}$$

$$W^*=D\vec{V}_r^*=\vec{X}^*+\vec{V}_r^*=DT^*+\mathrm{Bi}T^*+i\,\mathrm{Ma}_k\vec{k}\cdot\vec{X}^*=0 \quad \text{for } z=0\ . \tag{B8}$$

The resolution of the adjoint problem $S_k^*(V_k^*)=0$ (with $V_k^*\in E^*$) gives

$$V_k^*=\frac{-ke^{kz}}{4(2k+\mathrm{Bi})}\begin{bmatrix}i\vec{k}k^{-2}(1-kz-k^2z^2)\\z(1-kz)\\-4(1+kz)\\-8k\\-i\vec{k}k^{-2}\end{bmatrix}, \tag{B9}$$

where the normalization $\langle \vec{V}_k^*, \Theta_{\vec{k}}(U_k^0)\rangle=1$ has been adopted.

Finally, the eigenfunctions of the spectral problem (12) read

$$U_k^\sigma=\begin{bmatrix}\vec{V}_{rk}^\sigma\\W_k^\sigma\\p_k^\sigma\\T_k^\sigma\end{bmatrix}=-4k^2(k+\mathrm{Bi})\begin{bmatrix}i\vec{k}k^{-2}e^{kz}(1+kz)\\ze^{kz}\\2e^{kz}\\e^{kz}\left[2\dfrac{k}{\sigma^2}+\dfrac{z}{\sigma}\right]-2ke^{(\sigma+k^2)^{1/2}z}\left[\dfrac{1}{k^2\mathrm{Ma}}+\dfrac{1}{\sigma^2}\right]\end{bmatrix}, \tag{B10}$$

where the corresponding eigenvalue σ is solution of the dispersion relation (13). Note that the derivation of (B9) assumes $\sigma+k^2>0$ [which is verified provided $k<\mathrm{Ma}/2\ \mathrm{Bi}$, as seen from Eq. (13)]. Otherwise, when $\sigma+k^2<0$, imaginary roots are obtained from the characteristic relation and lead to a continuum of solutions bounded at $z\to-\infty$, but which do not satisfy boundary conditions (2).

APPENDIX C: CALCULATION OF THE MEAN TEMPERATURE PROFILE

For the roll mode $A_{\vec{k}}=a_1(t)\delta(\vec{k}-\vec{k}_0)+\bar{a}_1(t)\delta(\vec{k}+\vec{k}_0)$ (see the end of Sec. III), the $k=0$ Fourier component of the perturbation vector is found from (A5) as

$$U_{k=0}^D=2|a_1|^2U_{01}^D(z)\ , \tag{C1}$$

where, according to (A6), $U_{01}^D(z)$ is the solution of the inhomogeneous problem

$$\mathcal{L}_0(U_{01}^D)=N_{1,-1}(U_1^0,U_{-1}^0) \tag{C2}$$

since $M_{k=0}=0$ and the resonant part of $N_{1,-1}$ is zero, as $Z_{10}=0$ from (A3). Here again the subscripts refer to the mode number (1 for $\vec{k}_0$, -1 for $-\vec{k}_0$). It is computed that the only nonzero component of $U_{01}^D(z)$ is $T_{01}^D(z)$, the solution of

$$D^2T_{01}^D=W_1^0DT_{-1}^0-i\vec{k}_0\cdot\vec{V}_{r1}^0T_{-1}^0=D(W_1^0T_1^0)\ , \tag{C3}$$

where the neutral stability functions are given by (B2). Then, the solution belonging to E is

$$T_{01}^D=(5\,\mathrm{Bi}^2+12k_0\mathrm{Bi}+7k_0^2)\times\left[e^{2k_0z}\left[\frac{1}{2k_0}-z\right]-\frac{1}{2k_0}\right]+(\mathrm{Bi}+k_0)^2k_0e^{2k_0z}z^2(5-2k_0z)\ . \tag{C4}$$

The cubic coefficient Z_{111}^0 can then be computed from (A7) as

$$Z_{111}^0=-\langle V_1^*,N_{1,0}(U_1^0,U_{01}^D)\rangle=-\int_{-\infty}^0T_1^*(W_1^0)^2T_1^0dz=-\frac{k_0^2(\mathrm{Bi}+k_0)^2(3\,\mathrm{Bi}+5k_0)}{2(\mathrm{Bi}+2k_0)}\ . \tag{C5}$$

A slightly longer but similar computation leads to the expression of the second cubic coefficient Z_{-111}^0 and then finally to Eq. (20). Equation (27) is also obtained in this way, but by using eigenfunctions (B10) instead of the neutral stability functions (B2).

[1] F. Preisser, D. Schwabe, and A. Scharmann, J. Fluid Mech. **126**, 545 (1983).
[2] Y. Kamotani, J. H. Lee, S. Ostrach, and A. Pline, Phys. Fluids A **4**, 955 (1992).
[3] H. Bénard, Rev. Gen. Sci. Pures Appl. **11**, 1261 (1900).
[4] M. J. Block, Nature **178**, 650 (1956).
[5] H. Linde, P. Schwartz, and H. Wilke, in *Dynamics and Instability of Fluid Interfaces,* edited by T. S. Sorensen

(Springer-Verlag, Berlin, 1979), pp. 75–119.
[6] P. D. Weidman, H. Linde, and M. G. Velarde, Phys. Fluids A **4**, 921 (1992).
[7] C. V. Sternling and L. E. Scriven, AIChE J. **5**, 514 (1959).
[8] E. L. Koschmieder and M. I. Biggerstaff, J. Fluid Mech. **167**, 49 (1986).
[9] P. Cerisier, C. Jamond, J. Pantaloni, and C. Perez-Garcia, Phys. Fluids **30**, 954 (1987).
[10] J. K. Platten and J. C. Legros, *Convection in Liquids* (Springer-Verlag, Berlin, 1984).
[11] Ch. Normand, Y. Pomeau, and M. G. Velarde, Rev. Mod. Phys. **49**, 581 (1977).
[12] J. Pantaloni, R. Bailleux, J. Salan, and M. G. Velarde, J. Non-Equilib. Thermodyn. **4**, 201 (1979).
[13] J. R. A. Pearson, J. Fluid Mech. **4**, 489 (1958).
[14] J. W. Scanlon and L. A. Segel, J. Fluid Mech. **30**, 149 (1967).
[15] M. Bestehorn, Phys. Rev. E **48**, 3622 (1993).
[16] M. C. Cross and P. C. Hohenberg, Rev. Mod. Phys. **65**, 851 (1993).
[17] G. Dewel, P. Borckmans, A. De Wit, B. Rudovics, J.-J. Perraud, E. Dulos, J. Boissonade, and P. De Kepper, Physica A **213**, 181 (1995).
[18] S. Chandrasekhar, *Hydrodynamic and Hydromagnetic Stability* (Clarendon, Oxford, 1961).
[19] M. Fermigier, L. Limat, J. E. Wesfreid, P. Boudinet, and C. Quilliet, J. Fluid Mech. **236**, 349 (1992).
[20] F. H. Busse, Rep. Prog. Phys. **41**, 1929 (1978).
[21] D. A. Goussis and R. E. Kelly, Int. J. Heat Mass Transfer **33**, 2237 (1990).
[22] A. A. Golovin, A. A. Nepomnyashchy, and L. M. Pismen, Phys. Fluids **6**, 34 (1994).
[23] A. Cloot and G. Lebon, J. Fluid Mech. **145**, 447 (1984).
[24] J. Bragard and G. Lebon, Europhys. Lett. **21**, 831 (1993).
[25] S. Rosenblat, G. M. Homsy, and S. H. Davis, J. Fluid Mech. **120**, 91 (1982); **120**, 123 (1982).
[26] P. C. Dauby, G. Lebon, P. Colinet, and J. C. Legros, Q. J. Mech. Appl. Math. **46**, 683 (1993).
[27] A. Vidal and A. Acrivos, Phys. Fluids **9**, 615 (1966).
[28] P. Manneville, *Dissipative Structures and Weak Turbulence* (Academic, Boston, 1990).
[29] C. A. Jones and M. R. E. Proctor, Phys. Lett. A **121**, 224 (1987).
[30] M. R. E. Proctor and C. A. Jones, J. Fluid Mech. **188**, 301 (1988).
[31] W. V. R. Malkus, Proc. R. Soc. London Ser. A **225**, 196 (1954).
[32] F. H. Busse, in *Mantle Convection, Plate Tectonics and Global Dynamics,* edited by W. R. Peltier (Gordon and Breach, New York, 1989).
[33] S. Rosenblat, G. M. Homsy, and S. H. Davis, Phys. Fluids **24**, 2115 (1981).
[34] Ch. Karcher and U. Müller, Fluid Dyn. Res. **15** (1), 25 (1995).
[35] W. Eckhaus, *Studies in Nonlinear Stability Theory* (Springer, New York, 1965).
[36] R. Lefever and D. Carati, Physica A **213**, 90 (1995).
[37] L. M. Pismen and A. A. Nepomnyashchy, Europhys. Lett. **24**, 461 (1993).